

# Forensic Iris Image-Based Post-Mortem Interval Estimation

Rasel Ahmed Bhuiyan      Adam Czajka

Department of Computer Science and Engineering, University of Notre Dame  
384 Fitzpatrick Hall of Engineering, Notre Dame, 46556, Indiana, USA

{rbhuiyan, aczajka}@nd.edu

## Abstract

*Post-mortem iris recognition is an emerging application of iris-based human identification in a forensic setup. One factor that may be useful in conditioning iris recognition methods is the tissue decomposition level, which is correlated with the post-mortem interval (PMI), i.e. the number of hours that have elapsed since death. PMI, however, is not always available, and its precise estimation remains one of the core challenges in forensic examination. This paper presents the first known to us method of the PMI estimation directly from forensic iris images. To assess the feasibility of the iris-based PMI estimation, convolutional neural networks-based models (VGG19, DenseNet121, ResNet152, and Inception\_v3) were trained to predict the PMI from (a) near-infrared (NIR), (b) visible (RGB), and (c) multispectral forensic iris images. Models were evaluated following a 10-fold cross-validation, in (S1) sample-disjoint, (S2) subject-disjoint, and (S3) cross-dataset scenarios. We found that using the multispectral data offers a spectacularly low mean absolute error (MAE) of  $\approx 3.5$  hours in the scenario (S1), a bit worse MAE  $\approx 17.5$  hours in the scenario (S2), and MAE  $\approx 69.0$  hours in the scenario (S3). This suggests that if the environmental conditions are favorable (e.g., bodies are kept in low temperatures), forensic iris images provide features that are indicative of the PMI and can be automatically estimated. The source codes and model weights are made available with the paper.*

## 1. Introduction

Iris recognition, after demonstrating its capabilities to serve as a biometric identifier up to a few weeks after death, and with development of government-led datasets of iris images, such as the FBI's Next Generation Identification [1], it has been observing an increased interest in forensic applications. Iris recognition can serve as an element of the forensic toolkit, aiding in cold case resolutions, or a stan-

dalone method allowing for quick and accurate registering bodies in mass fatality incidents [2].

The post-mortem interval (PMI), while not allowing for direct person's identification, may play an important role in (a) narrowing down the time frame within which the individual likely died and was left at the scene (what directly facilitates biometric 1:N matching), and (b) conditioning iris recognition methods by the PMI to allow for different processing of the iris pattern depending on the severity of iris tissue decomposition, which is correlated with the PMI. This paper makes the first known to us attempt to assess the feasibility of the PMI estimation from post-mortem iris images, and offers methods for such iris image-based PMI assessment. More specifically, the paper makes the following **novel contributions**:

- (a) deep learning-based **models** (utilizing VGG19, DenseNet121, ResNet152, and Inception\_v3 architectures) **estimating the PMI** from either near infrared (NIR) ISO/IEC 19794-6-compliant iris images, or visible-light (RGB) iris images,
- (b) a **fusion model**, which combines NIR image- and RGB image-based predictions, if such multispectral forensic iris images are available,
- (c) **very rigorous cross-validation experiments**, in which multiple models are independently trained and tested on 15,279 forensic iris images originating from 348 deceased subjects, in three scenarios:
  - (S1) sample-disjoint (but not subject- or dataset-disjoint),
  - (S2) subject-disjoint (thus also sample-disjoint, but not dataset-disjoint), and
  - (S3) dataset-disjoint (thus also sample- and subject-disjoint).
- (d) **model weights and sources codes** to facilitate an immediate use of the designed models<sup>1</sup>.

<sup>1</sup><https://github.com/rabhuiyan/PMI-Estimation>

The scenario (S3) simulates the most realistic situation when train and test data originate from different subjects, environmental conditions and acquisition procedures. In this challenging scenario, the best model utilizing the multispectral iris images (NIR+RGB) achieves the Mean Absolute Error (MAE) of 71.48 ( $\pm 1.15$ ) hours, or approx. 3 days. In a more favorable, but still subject-disjoint scenario (S2), in which the acquisition procedures are similar, the best model's MAE = 17.52 ( $\pm 17.19$ ) hours, so less than a day. Given that no other information than the iris image is available, these results are very encouraging and may contribute to a multi-modal PMI estimation if other type of data or information about the case are known.

## 2. Related Works

### 2.1. Forensic Iris Recognition

For a considerable duration, the scientific and industrial communities have held the notion that iris recognition is challenging or even impossible to perform after a person's death. This belief is exemplified by Daugman's assertion in a 2001 BBC interview, where he highlighted that "shortly after death, the pupil dilates and the cornea becomes cloudy," rendering iris recognition problematic [3]. Similarly, Szczepanski et al. [4] claimed that "the iris decays within a few minutes after death," indicating a rapid degradation process. Moreover, certain commercial sources have asserted the scientific impossibility of utilizing a deceased individual's iris for recognition due to factors such as the relaxation of the iris muscle after death, resulting in a fully dilated pupil with no discernible iris texture. Consequently, it has been widely accepted that the lack of usable iris area [5] or the disappearance of iris features alongside pupil dilation [6] renders a deceased person's iris unsuitable for recognition purposes. However, recent investigations suggest that the decomposition of the eye and iris is more complex and slower than previously presumed.

For instance, Bolme et al. [7] were the pioneers in examining the post-mortem biometric performance of face, fingerprint, and iris recognition in outdoor environments. Their findings revealed that while fingerprints and faces showed moderate resilience to decomposition, iris recognition suffered rapid degradation. The correct verification rate dropped significantly, approaching zero after 14 days of outdoor exposure. A subsequent investigation by Sauerwein et al. [8] demonstrated that irises can remain readable for up to 34 days post-mortem when cadavers are subjected to low temperatures during winter. Notably, human examiners were asked to match image pairs instead of using iris recognition algorithms. These findings suggest that exposing a cadaver to low temperatures in winter can increase the probability of correctly identifying an iris, even if it has been outside for an extended period.

A recent investigation by Trokielewicz et al. [9] suggests that post-mortem iris recognition may achieve close-to-perfect accuracy approximately 5–7 hours after death, and in some cases, remains viable even up to 21 days post-mortem. These findings challenge past assertions in the literature regarding the rapid degradation of the iris shortly after death, indicating that the dynamics of post-mortem changes to the iris, crucial for biometric identification, are more moderate than previously thought.

### 2.2. Post-mortem Interval Estimation

Estimating the post-mortem interval remains one of the most needed and challenging tasks in forensic sciences. It typically relies on physical postmortem alterations like cooling [10, 11, 12, 13], stiffening [14, 15, 16, 17], and decomposition [18, 19, 20, 21], as well as chemical changes such as electrolyte modifications in body fluids [22, 23, 24, 25, 26]. Forensic entomology has also been explored as a means to predict the PMI, involving the examination of insects' presence, age, and timing of insects' incidence on corpses [27, 28]. Furthermore, various techniques utilizing signal and image processing methods have been suggested for PMI estimation. Canturk *et al.* [29] investigated the relationship between tissue conductivity changes and the time of death. Several studies have highlighted the potential of postmortem opacity development in the eye as a tool for estimating PMI. Kumar *et al.* [30] provided insights into corneal opacity development based on personal observations, while Zhou *et al.* [31] and Liu *et al.* [32] conducted studies on postmortem eye changes in rabbits, utilizing image processing methods for feature extraction and classification. Kawashima *et al.* [33] investigated human subjects, employing RGB pixel values of corneal regions and developing a mathematical formula for the PMI calculation. Additionally, Canturk *et al.* [34] analyzed eye images from ten human subjects over a 15-hour period, medically interpreting postmortem alterations of the eye.

To our knowledge, no study has yet investigated the PMI estimation directly from biometric iris images, and this paper proposes and evaluates the first such models, being able to assess the PMI from either biometric (ISO/IEC 19794-6-compliant) or visible-light iris images.

## 3. Methodology

### 3.1. Datasets

To conduct this research, we have compiled a dataset of 8,064 NIR and 7,215 RGB forensic iris images derived from 348 subjects. At the time of preparing this paper, and to our knowledge, this is the largest dataset of forensic iris images that one can compile from publicly-available sources, which are characterized shortly below.

**Warsaw BioBase Post Mortem Iris v2.0** [9] includes

1,787 RGB and 1,200 NIR iris images sourced from 37 deceased individuals during from 1 to 13 acquisition sessions spanning 5 to 814 hours post-mortem. The data was collected in a hospital mortuary setting, and an ambient temperature was kept at approximately 6° Celsius (42.8° Fahrenheit). Other details regarding pre-cold storage conditions, air pressure, and humidity, are unknown.

**Warsaw BioBase Post Mortem Iris v3.0** [35], comprises 785 RGB and 1,094 NIR images sourced from 42 deceased individuals, spanning up to 369 hours post-mortem. The environmental conditions mirror those known for the Warsaw BioBase Post Mortem Iris v2.0 dataset.

**NIJ-2018-DU-BX-0215** [36], stands as the most recent and extensive forensic iris dataset collected to date. It includes 4,643 RGB and 5,770 NIR images acquired from 269 deceased individuals, with PMI spanning up to 1,674 hours post-mortem.

We will call all samples from the **Warsaw BioBase Post Mortem Iris v2.0** and **Warsaw BioBase Post Mortem Iris v3.0** datasets combined as **Warsaw**, since all these samples were collected in the same environment. Also for the sake of brevity, we will call **NIJ-2018-DU-BX-0215** as **NIJ**.

Fig. 1 illustrates how iris image (and iris pattern specifically) changes when PMI grows. It is also important to note that the PMI distributions in Warsaw and NIJ datasets are different. It is evident from Fig. 2 that the NIJ dataset includes samples from a more diverse range of the PMI.

### 3.2. PMI Estimation Models

We explore four convolutional neural networks (CNN) backbones to build regression models estimating the PMI: VGG19 [37], DenseNet121 [38], ResNet152 [39], and Inception V3 [40]. Additionally, to discern the most effective strategy for PMI estimation, the proposed models utilize (1) only NIR samples, (2) only RGB samples, and (3) a multi-spectral approach in which both NIR and RGB samples are used (assuming their availability from the same subjects). These three approaches are characterized briefly below.

In our narrow-band spectral models (NIR and RGB, considered individually), we modified the last (classification) layer for the models fed with RGB images, while for the models utilizing NIR samples, we modified both the first and last layers of each backbone. This was needed to adapt the model backbones to the regression task, and to different number of channels in NIR and RGB images.

Our multi-spectral models (NIR and RGB samples combined) consist of two separate models:  $f_{\text{NIR}}$  dedicated to processing NIR data and  $f_{\text{RGB}}$  processing the RGB data. Both models employ the same model architectures used in narrow-band spectral models, ensuring a consistent approach across different modalities. The PMI prediction  $\hat{y}$  is made by a simple two-layer perceptron, put on top of concatenated embeddings extracted by  $f_{\text{NIR}}$  and  $f_{\text{RGB}}$ , namely:

$$\hat{y} = \mathbf{W}_2 \sigma(\mathbf{W}_1(\mathbf{f}_{\text{NIR}} \oplus \mathbf{f}_{\text{RGB}}) + \mathbf{b}_1) + b_2 \quad (1)$$

where  $\oplus$  is a vector concatenation operator,  $\mathbf{W}_1$  and  $\mathbf{W}_2$  are weight matrix and vector,  $\mathbf{b}_1$  is the bias vector,  $b_2$  is a scalar bias term, and  $(\sigma)$  is a ReLU activation function.

### 3.3. Data Preprocessing and Augmentation

In this study, we center-cropped iris images to a square image of  $224 \times 224$  pixels (in case of VGG19, DenseNet121, and ResNet152 backbones) or  $229 \times 229$  pixels (in case of Inception\_v3 backbone). There are two reasons of using cropped images. First, the periocular regions of post-mortem irises include features, such as metal retractors used to increase the palpebral fissure, that may be accidentally correlated with the PMI, and picked by the models. Secondly, we were interested in applying pre-trained models due to sparse and small datasets of post-mortem iris images that the community has at hand right now, what makes training the models from scratch more challenging.

Standard augmentations were applied to the training samples, such as random horizontal flipping, random rotation within a range of -30 to 30 degrees, random brightness, contrast, and sharpness adjustments.

### 3.4. Performance Evaluation and Metrics

We evaluate our models using three distinct scenarios: **(S1) sample-disjoint** 10-fold cross-validation, **(S2) subject-disjoint** 10-fold cross-validation, and **(S3) cross-dataset** evaluation. To ensure a fair comparison, we fixed the training and testing datasets across all models during experimentation.

In all training experiments, we used Adam optimizer with a batch size of 20, a learning rate of 1e-4, and a weight decay of 1e-6. We trained each model for 500 epochs.

To assess the effectiveness of the proposed PMI estimation model, we calculate Root-mean Square Error (RMSE) and Mean Absolute Error (MAE) between the ground truth PMI and predicted PMI.

## 4. Experiments and Results

### 4.1. Sample-disjoint Evaluation (S1)

In this scenario, we assess the performance of our models using a sample-disjoint 10-fold cross-validation approach. This is the most favorable scenario, in which we assume that (a) previous data, although with different PMIs, from the same subjects is available, and (b) the acquisition environment (*e.g.*, sensors, ambient temperature, technicians collecting the data) is the same in case of training and test samples. This scenario S1 sets the lower bound for the errors in estimating the PMI solely from the iris image.

Tables 1, 2, and 3 provide a comparative analysis of the PMI estimation model’s average performance, measured

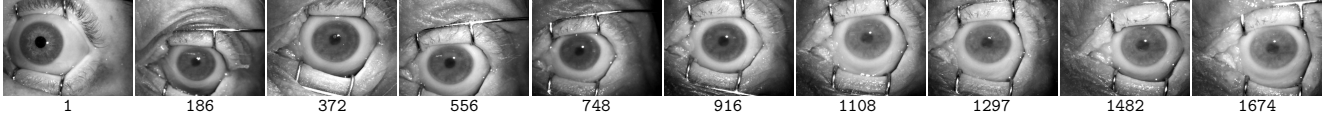


Figure 1. Example post-mortem iris samples collected at different post-mortem intervals (shown underneath the images).

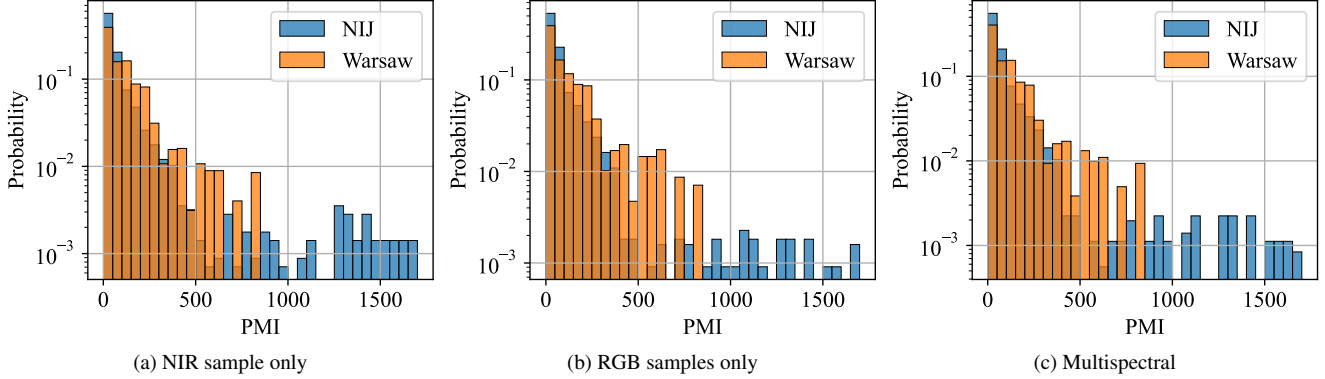


Figure 2. PMI distributions for the Warsaw and NIJ datasets for NIR-only samples, RGB-only samples, and NIR and RGB samples (pairs taken from the same eye) combined.

Table 1. PMI (in hours) estimated on the **NIR data** and averaged across **sample-disjoint** 10-fold cross-validation experiments.

Model Backbone	RMSE		MAE	
	Mean	StDev	Mean	StDev
VGG19	9.31	8.32	5.04	2.62
Inception_v3	92.00	14.07	56.35	7.78
DenseNet121	7.18	7.14	4.10	2.74
ResNet152	7.52	7.15	4.20	2.12

Table 2. Same as in Tab. 1, except that **RGB data** was used.

Model Backbone	RMSE		MAE	
	Mean	StDev	Mean	StDev
VGG19	18.09	11.87	9.24	3.34
Inception_v3	69.32	18.98	38.43	4.09
DenseNet121	14.32	18.01	5.75	3.39
ResNet152	19.29	11.66	5.77	3.30

Table 3. Same as in Tab. 1, except that **multispectral data** was used.

Model Backbone	RMSE		MAE	
	Mean	StDev	Mean	StDev
VGG19	9.32	8.11	5.40	3.67
Inception_v3	38.59	4.32	20.37	1.91
DenseNet121	6.16	7.01	3.56	3.09
ResNet152	6.18	4.79	3.44	2.28

in hours, across different model backbones for NIR-only, RGB-only, and multispectral data, respectively. For the NIR data (Tab. 1), the DenseNet121 backbone achieves the low-

est RMSE (**7.18 hours**) and MAE (**4.10 hours**) among the models, indicating superior performance in estimating the PMI for NIR spectral data. Conversely, the Inception\_v3 backbone exhibits significantly higher RMSE (**92.00 hours**) and MAE (**56.35 hours**) compared to other models, suggesting less accurate PMI estimates for NIR data.

Similarly, for RGB data (Tab. 2), the DenseNet121 backbone again demonstrates the lowest RMSE (**14.32 hours**) and MAE (**5.75 hours**), while Inception\_v3 backbone once more exhibits higher RMSE (**69.32 hours**) and MAE (**38.43 hours**).

Finally, in the case of multispectral data (Tab. 3), the ResNet152 backbone achieves the lowest RMSE (**6.18 hours**) and MAE (**3.44 hours**) while the Inception\_v3 backbone performing better compared to its performance with NIR and RGB data individually, still exhibits higher RMSE (**38.59 hours**) and MAE (**20.37 hours**).

In Figure 3, we observe distinct patterns among the backbone models. Specifically, the VGG19, DenseNet121, and ResNet152 models demonstrate the accurate estimation of higher PMI. However, these models exhibit a few discrepancies in their estimations for lower PMI and the differences between the predicted and actual PMI are consistently small within the entire PMI range. The Inception\_v3 model more often overestimates and underestimates the PMI specially for a higher PMI range. Similar scatter plots for NIR and RGB data are included in the Supplementary Materials (Figures A5 and A6).

This spectacularly good performance in PMI estimation (with errors for the best model not exceeding 4 hours) is due to two factors. First, as mentioned above, is the non-subject-disjoint train-test protocol. Second, as demonstrated in Fig.

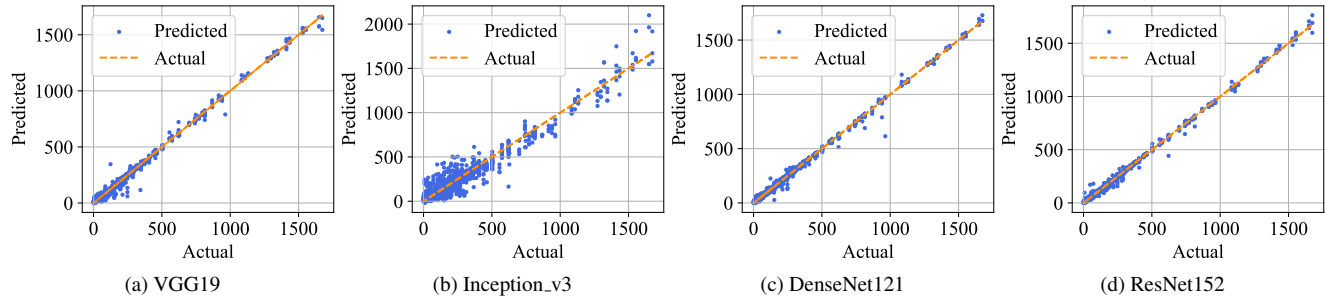


Figure 3. Scatter plots visualizing the predicted PMI values against the actual PMI values for **multispectral data** combined for all **sample-disjoint** 10-fold cross-validations.

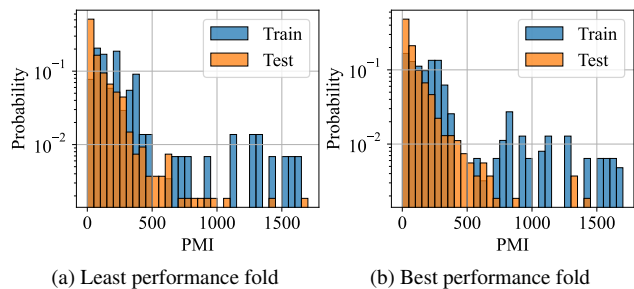


Figure 4. Comparison of the PMI distributions between training and test datasets for the least (a) and best (b) performing folds observed in the **sample-disjoint** 10-fold cross-validation for the **multispectral data**.

4, is the wider range of the PMI in the training set compared to the test set, for both the worst model and the best model obtained in 10-fold train-test cross-validation. Figures A1 and 4 for NIR and RGB data, separately, show very similar trends, and where thus included in the Supplementary Materials.

## 4.2. Subject-disjoint Evaluation (S2)

In this scenario, we examine the performance of our models under a subject-disjoint 10-fold evaluation setup. This evaluation approach involves partitioning the combined datasets (Warsaw and NIJ) so that samples from each subject are exclusively present in either the training or the test set, what makes it more realistic than scenario S1. This scenario assumes, as in S1, that acquisition environment is uniform across the train and test data collections.

Table 4. PMI (in hours) estimated on the **NIR data** and averaged across **subject-disjoint** 10-fold cross-validation experiments.

Model Backbone	RMSE		MAE	
	Mean	StDev	Mean	StDev
VGG19	55.54	56.85	32.35	24.72
Inception_v3	115.07	67.46	68.79	31.95
DenseNet121	31.23	30.20	19.67	16.14
ResNet152	45.53	47.68	26.49	21.98

Table 5. Same as in Tab. 4, except that **RGB data** was used.

Model Backbone	RMSE		MAE	
	Mean	StDev	Mean	StDev
VGG19	47.96	35.35	27.20	15.72
Inception_v3	77.74	40.78	45.90	19.75
DenseNet121	50.53	28.13	33.90	16.64
ResNet152	52.14	46.98	30.91	21.36

Table 6. Same as in Tab. 4 for **multispectral data**.

Model Backbone	RMSE		MAE	
	Mean	StDev	Mean	StDev
VGG19	29.00	29.71	17.52	17.19
Inception_v3	56.33	22.75	32.42	12.93
DenseNet121	31.86	28.74	19.69	14.98
ResNet152	30.72	28.62	20.02	19.01

Tables 4, 5, and 6 compare the PMIs estimated by all model architectures for NIR-only, RGB-only, and multispectral data, respectively. For the NIR data (Tab. 4), the DenseNet121 backbone achieves the lowest RMSE (**31.23 hours**) and MAE (**19.67 hours**) among the models. Conversely, the Inception\_v3 backbone exhibits significantly higher RMSE (**115.07 hours**) and MAE (**68.79 hours**) compared to other models, suggesting less accurate PMI estimates for NIR data.

Similarly, for RGB data (Tab. 5), the VGG19 backbone demonstrates the lowest RMSE (**47.96 hours**) and MAE (**27.20 hours**), while Inception\_v3 backbone once more exhibits higher RMSE (**77.74 hours**) and MAE (**45.90 hours**).

In the case of multispectral data (Tab. 6), the VGG19 backbone achieves the lowest RMSE (**29.00 hours**) and MAE (**17.52 hours**) while the Inception\_v3 backbone performing better compared to its performance with NIR and RGB data individually, still exhibits higher RMSE (**56.33 hours**) and MAE (**32.42 hours**). The trends observed in Figure 5 are similar across almost all model backbones, which tend to underestimate the PMI, especially for higher actual PMI values. Inception\_v3, however, occasionally

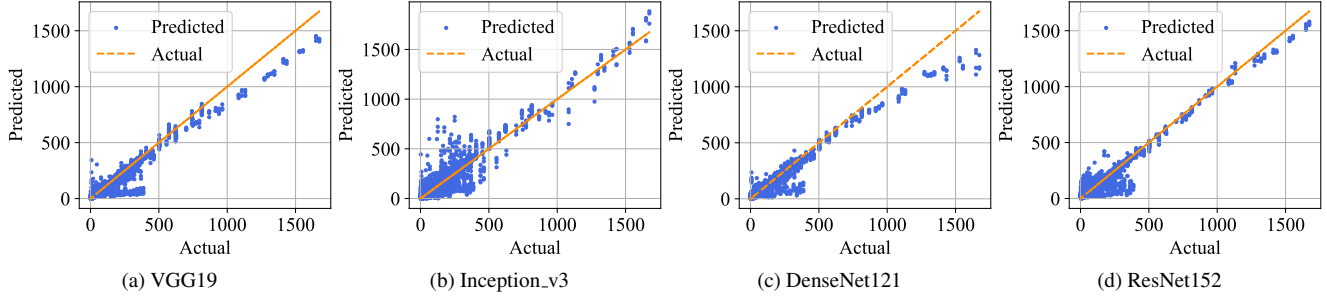


Figure 5. Scatter plots visualizing the predicted PMI values against the actual PMI values for **multispectral data** combined for all **subject-disjoint** 10-fold cross-validations.

overestimates the PMI for higher PMI ranges. One potential explanation is the scarcity of data with PMIs larger than 1000 hours, making it difficult for the models to learn features associate with iris pattern decomposition for such high PMIs. These observations are very similar to models trained solely on NIR or RGB data, and thus the scatter plots for these cases were included in the supplementary materials (Figures A7 and A8).

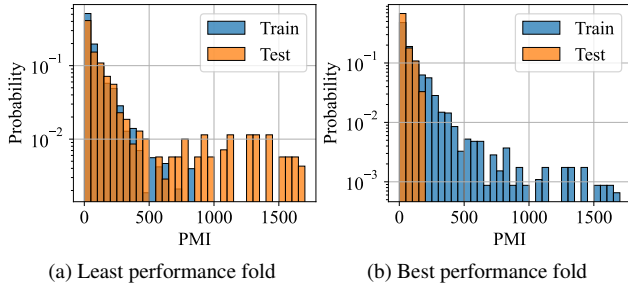


Figure 6. Comparison of the PMI distributions between training and test datasets for the least (a) and best (b) performing folds observed in the **subject-disjoint** 10-fold cross-validation for the **multispectral data**.

Fig. 6 illustrates how PMI distributions in training and test datasets differ when we look at folds in which the best or the worst results were obtained (for multispectral data). The least-performing fold included test samples with a wider PMI range compared to train samples, while the best-performing fold has an opposite relationship. This confirms the hypothesis that large variation of the PMI in the training set is a key factor in obtaining good performance. An identical observation has been made for models trained with the NIR and RGB data, separately (hence corresponding Figures A3 and A4 are added to the supplementary materials).

### 4.3. Cross-dataset Evaluation (S3)

In this scenario, we evaluate the performance of the models in a training regime which is both subject-disjoint and dataset-disjoint. This scenario thus does not assume knowledge of the acquisition environment, what makes it the most

realistic across all scenarios considered in this work. Each model is trained five times under the same settings.

Tab. 7 compares models trained on the NIJ dataset and tested on the Warsaw dataset. Among these models, ResNet152 achieves the lowest RMSE (**105.62 hours**) and MAE (**71.48 hours**). Tab. 10 compares models after swapping the datasets, that is, models are trained on the Warsaw dataset and tested on the NIJ dataset, where ResNet152 also demonstrates the lowest RMSE (**163.27 hours**) and MAE (**76.36 hours**), showcasing consistent performance across datasets.

Table 7. PMI (in hours) estimated on the **NIR data** by models trained on NIJ dataset and **tested on Warsaw** dataset.

Model Backbone	RMSE		MAE	
	Mean	StDev	Mean	StDev
VGG19	112.71	2.61	73.14	1.58
Inception_v3	118.18	3.02	78.76	2.07
DenseNet121	112.20	2.08	72.36	1.46
ResNet152	105.62	3.04	71.48	1.15

Table 8. Same as in Tab. 7 for **RGB data**.

Model Backbone	RMSE		MAE	
	Mean	StDev	Mean	StDev
VGG19	106.07	2.79	88.58	1.99
Inception_v3	90.14	2.78	73.23	2.05
DenseNet121	99.68	1.59	82.32	1.07
ResNet152	98.18	2.26	81.15	2.27

Table 9. Same as in Tab. 7 for **multispectral data**.

Model Backbone	RMSE		MAE	
	Mean	StDev	Mean	StDev
VGG19	107.68	5.44	69.58	2.64
Inception_v3	109.82	3.62	69.22	0.83
DenseNet121	112.74	2.50	70.04	1.36
ResNet152	111.31	6.49	69.12	2.16

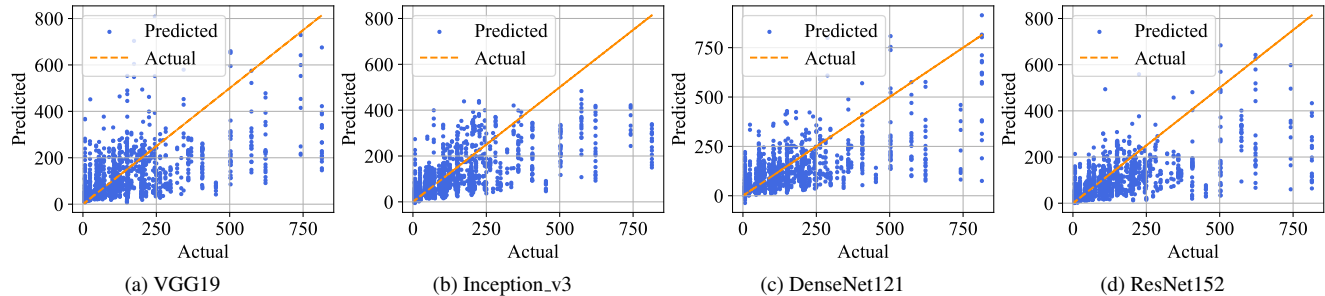


Figure 7. Scatter plots visualizing the predicted PMI values against the actual PMI values for **multispectral data** by models trained on the NIJ dataset and **tested on the Warsaw dataset**.

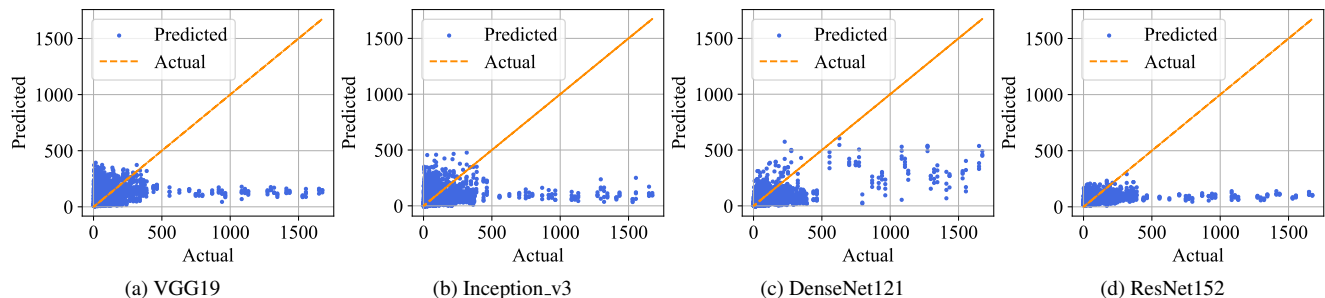


Figure 8. Scatter plots visualizing the predicted PMI values against the actual PMI values for **multispectral data** by models trained on the Warsaw dataset and **tested on the NIJ dataset**.

Table 10. PMI (in hours) estimated on the **NIR data** by models trained on Warsaw dataset and **tested on NIJ** dataset.

Model Backbone	RMSE		MAE	
	Mean	StDev	Mean	StDev
VGG19	165.37	4.39	76.67	0.98
Inception_v3	170.66	6.26	80.83	2.80
DenseNet121	171.38	2.43	77.82	0.81
ResNet152	163.27	6.19	76.36	1.37

Table 11. Same as in Tab. 10 for **RGB data**.

Model Backbone	RMSE		MAE	
	Mean	StDev	Mean	StDev
VGG19	98.34	2.97	80.59	1.87
Inception_v3	97.34	3.04	81.10	3.39
DenseNet121	95.24	2.93	76.32	1.31
ResNet152	95.31	4.26	80.11	2.67

Table 12. Same as in Tab. 10 for **multispectral data**.

Model Backbone	RMSE		MAE	
	Mean	StDev	Mean	StDev
VGG19	152.56	3.49	85.46	6.14
Inception_v3	152.82	4.19	81.32	5.52
DenseNet121	136.00	4.46	68.55	0.73
ResNet152	152.63	3.36	77.66	3.90

Tab. 8 illustrates the results for models trained with RGB data only. Again, we first train on the NIJ dataset and test on the Warsaw dataset, where Inception\_v3 stands out with the lowest RMSE (**90.14 hours**) and MAE (**73.23 hours**). Next, after dataset swap, the models are trained on the Warsaw dataset and tested on the NIJ dataset (Tab. 11). In this case DenseNet121 demonstrates the lowest RMSE (**95.24 hours**) and MAE (**76.32 hours**).

Finally, Tables 9 and 12 illustrate analogous experiments when multispectral data is used. In these cases ResNet152 and DenseNet121 achieve the lowest RMSE (**111.31 hours** when trained on the NIJ dataset, and **136.00 hours** when trained on the Warsaw dataset) and MAE (**69.12 hours** when trained on the NIJ dataset, and **68.55 hours** when trained on the Warsaw dataset).

## 5. Discussion

Our study delved, to our knowledge for the first time, into the feasibility of using solely iris-based data for estimating the PMI, employing deep learning models trained on forensic iris images representing various spectral bands. Our findings suggest that the PMI estimation, particularly with multispectral data, is feasible and its usefulness depends on the required accuracy.

The first observation made in this study is that dataset-disjoint train-test regime (S3) allows to train models that are almost two orders of magnitude worse than those obtained in sample-disjoint setup (S1), and approx. four times worse



than in those trained according to the subject-disjoint train-test protocol (S2). This shows how difficult the automatic estimation of the PMI can be if one poses solely the iris image. The exceptionally low MAE of  $\approx 3.5$  hours achieved in the sample-disjoint scenario (S1) can be attributed to several factors. Having the same-subject data in both training and test sets enables the model to capture the unique characteristics of individuals, resulting in more accurate PMI estimation. Moreover, the PMI distribution may align closely between the training and testing data.

The second observation from this study is that a narrower range of PMI for samples included into Warsaw data (cf. Fig. 2) results in significantly worse models, what is illustrated in scatter plots 7 and 8: models trained solely on the Warsaw samples (see Fig. 8) are unable to predict correct PMI on the NIJ dataset, while models trained solely on the NIJ samples (see Fig. 7) present much better capabilities to predict the PMI on the Warsaw dataset. These observations, made for multispectral data-based training, are true also for models trained with NIR and RGB data, and the corresponding plots are included in the supplementary materials (Figures A9, A10, A11 and A12).

**Applications:** This is the first-of-its-kind attempt to use solely the iris image to estimate the PMI. One direct and obvious application is to serve as an element of the forensic toolkit, in which the PMI estimation may integrate several approaches, including those not related to the use of biometric data. The second, biometrics-related application, is to use the estimated PMI in conditioning post-mortem iris recognition methods, which were proposed in the past [41, 42, 2] but without considering PMI as a factor guiding the classifiers to using different features depending on the decomposition state.

**Limitations and Future Work:** A couple of limitations warrant acknowledgment.

First, relying solely on iris images may overlook crucial contextual factors like ambient temperature fluctuations or post-mortem changes in other tissues, potentially compromising estimation accuracy. Addressing this by incorporating additional contextual information could enhance the robustness of our models.

Second, generalization from our findings may be hampered by the dataset limited size and diversity despite rigorous cross-validation. A more expansive dataset encompassing diverse demographic characteristics, environmental conditions, and post-mortem states would bolster the validity and applicability of our results. This, certainly, is difficult to offer due to exceptionally arduous collection of forensic iris images. However, recent growth of generative models, including those designed specifically for post-mortem iris images [43], may partially mitigate this plight.

## References

- [1] FBI Next Generation Identification (NGI). <https://le.fbi.gov/science-and-lab/biometrics-and-fingerprints/biometrics/next-generation-identification-ngi>. Accessed: March 24, 2024.
- [2] A. Boyd, S. Yadav, T. Swearingen, A. Kuehlkamp, M. Trokielewicz, E. Benjamin, P. Maciejewicz, D. Chute, A. Ross, P. Flynn, K. Bowyer, and A. Czajka. Post-Mortem Iris Recognition – A Survey and Assessment of the State of the Art. *IEEE Access*, 8:136570–136593, 2020.
- [3] J. Daugman. Bbc news: The eyes have it. <http://news.bbc.co.uk/2/hi/science/nature/1477655.stm>, 2001. [Accessed: 2021-08-14].
- [4] A. Szczepański, K. Misztal, and K. Saeed. Pupil and iris detection algorithm for near-infrared capture devices. In *Computer Information Systems and Industrial Management: 13th IFIP TC8 International Conference, CISIM 2014, Ho Chi Minh City, Vietnam, November 5-7, 2014. Proceedings 14*, pages 141–150. Springer, 2014.
- [5] IrisGuard. Eyebank solution. <http://www.irisguard.com/eyebank/downloads/EyeBankPer%20Page.pdf>, 2016. [accessed: Jan 2016].
- [6] IriTech. Biometric access control can iris biometric enhance better security? <http://www.iritech.com/blog/iris-biometric-access-control>, August 20, 2015. [accessed: January 16, 2016].
- [7] D. S. Bolme, R. A. Tokola, C. B. Boehnen, T. B. Saul, K. A. Sauerwein, and D. W. Steadman. Impact of environmental factors on biometric matching during human decomposition. In *2016 IEEE 8th International Conference on Biometrics Theory, Applications and Systems (BTAS)*, pages 1–8. IEEE, 2016.
- [8] K. Sauerwein, T. B. Saul, D. W. Steadman, and C. B. Boehnen. The effect of decomposition on the efficacy of biometrics for positive identification. *Journal of Forensic Sciences*, 62(6):1599–1602, 2017.
- [9] M. Trokielewicz, A. Czajka, and P. Maciejewicz. Iris recognition after death. *IEEE Transactions on Information Forensics and Security*, 14(6):1501–1514, 2018.
- [10] M. Kaliszan, R. Hauser, and G. Kernbach-Wightton. Estimation of the time of death based on the assessment of post mortem processes with emphasis on body cooling. *Legal Medicine*, 11(3):111–117, 2009.
- [11] M. R. Rodrigo. Time of death estimation from temperature readings only: A laplace transform approach. *Applied Mathematics Letters*, 39:47–52, 2015.
- [12] Y. Igari, Y. Hosokai, and M. Funayama. Rectal temperature-based death time estimation in infants. *Legal Medicine*, 19:35–42, 2016.
- [13] M. R. Rodrigo. A nonlinear least squares approach to time of death estimation via body cooling. *Journal of Forensic Sciences*, 61(1):230–233, 2016.
- [14] L. Varetto and O. Curto. Long persistence of rigor mortis at constant low temperature. *Forensic Science International*, 147(1):31–34, 2005.



- [15] M. Ozawa, K. Iwadate, S. Matsumoto, K. Asakura, E. Ochiai, and K. Maebashi. The effect of temperature on the mechanical aspects of rigor mortis in a liquid paraffin model. *Legal Medicine*, 15(6):293–297, 2013.
- [16] A. Nishida, H. Funaki, M. Kobayashi, Y. Tanaka, Y. Akasaka, T. Kubo, and H. Ikegaya. Blood creatinine level in postmortem cases. *Science & Justice*, 55(3):195–199, 2015.
- [17] P. A. Martins, F. Ferreira, R. Natal Jorge, M. Parente, and A. Santos. Necromechanics: death-induced changes in the mechanical properties of human tissues. *Proceedings of the Institution of Mechanical Engineers, Part H: Journal of Engineering in Medicine*, 229(5):343–349, 2015.
- [18] A. A. Vass, S.-A. Barshick, G. Sega, J. Caton, J. T. Skeen, J. C. Love, and J. A. Synsteliën. Decomposition chemistry of human remains: a new methodology for determining the postmortem interval. *Journal of Forensic Sciences*, 47(3):542–553, 2002.
- [19] M. T. Ferreira and E. Cunha. Can we infer post mortem interval on the basis of decomposition rate? a case from a portuguese cemetery. *Forensic Science International*, 226(1-3):298–e1, 2013.
- [20] D. L. Cockle and L. S. Bell. Human decomposition and the reliability of a ‘universal’ model for post mortem interval estimations. *Forensic Science International*, 253:136–e1, 2015.
- [21] J. K. Suckling, M. K. Spradley, and K. Godde. A longitudinal study on human outdoor decomposition in central texas. *Journal of Forensic Sciences*, 61(1):19–25, 2016.
- [22] H. Chandrakanth, T. Kanchan, B. Balaraj, H. Virupaksha, and T. Chandrashekar. Postmortem vitreous chemistry—an evaluation of sodium, potassium and chloride levels in estimation of time since death (during the first 36 h after death). *Journal of Forensic and Legal Medicine*, 20(4):211–216, 2013.
- [23] C. Cordeiro, R. Seoane, A. Camba, E. Lendoiro, M. S. Rodríguez-Calvo, D. N. Vieira, and J. I. Muñoz-Barús. The application of flow cytometry as a rapid and sensitive screening method to detect contamination of vitreous humor samples and avoid miscalculation of the postmortem interval. *Journal of Forensic Sciences*, 60(5):1346–1349, 2015.
- [24] B. Zilg, S. Bernard, K. Alkass, S. Berg, and H. Druid. A new model for the estimation of time of death from vitreous potassium levels corrected for age and temperature. *Forensic science international*, 254:158–166, 2015.
- [25] A. K. Parmar and S. K. Menon. Estimation of postmortem interval through albumin in csf by simple dye binding method. *Science & Justice*, 55(6):388–393, 2015.
- [26] T. Rognum, S. Holmen, M. Musse, P. Dahlberg, A. Stray-Pedersen, O. Saugstad, and S. Opdal. Estimation of time since death by vitreous humor hypoxanthine, potassium, and ambient temperature. *Forensic Science International*, 262:160–165, 2016.
- [27] F. Tuccia, G. Giordani, and S. Vanin. A combined protocol for identification of maggots of forensic interest. *Science & Justice*, 56(4):264–268, 2016.
- [28] L. Iancu, T. Sahlean, and C. Purcarea. Dynamics of necrophagous insect and tissue bacteria for postmortem interval estimation during the warm season in romania. *Journal of Medical Entomology*, 53(1):54–66, 2016.
- [29] İ. Cantürk, F. Karabiber, S. Çelik, M. F. Şahin, F. Yağmur, and S. Kara. An experimental evaluation of electrical skin conductivity changes in postmortem interval and its assessment for time of death estimation. *Computers in Biology and Medicine*, 69:92–96, 2016.
- [30] B. Kumar, V. Kumari, T. Mahto, A. Sharma, and A. Kumar. Determination of time elapsed since death from the status of transparency of cornea in ranchi in different weathers. *Journal of Indian Academy of Forensic Medicine*, 34(4):336–338, 2012.
- [31] L. Zhou, Y. Liu, L. Liu, L. Zhuo, M. Liang, F. Yang, L. Ren, and S. Zhu. Image analysis on corneal opacity: a novel method to estimate postmortem interval in rabbits. *Journal of Huazhong University of Science and Technology [Medical Sciences]*, 30:235–239, 2010.
- [32] F. Liu, S. Zhu, Y. Fu, F. Fan, T. Wang, and S. Lu. Image analysis of the relationship between changes of cornea and postmortem interval. In *PRICAI 2008: Trends in Artificial Intelligence: 10th Pacific Rim International Conference on Artificial Intelligence, Hanoi, Vietnam, December 15-19, 2008. Proceedings 10*, pages 998–1003. Springer, 2008.
- [33] W. Kawashima, K. Hatake, R. Kudo, M. Nakanishi, S. Tamaki, S. Kasuda, and A. Ishitani. Estimating the time after death on the basis of corneal opacity. *Journal of Forensic Research*, 6(1):269, 2015.
- [34] İ. Cantürk, S. Çelik, M. F. Şahin, F. Yağmur, S. Kara, and F. Karabiber. Investigation of opacity development in the human eye for estimation of the postmortem interval. *Biocybernetics and Biomedical Engineering*, 37(3):559–565, 2017.
- [35] M. Trokielewicz, A. Czajka, and P. Maciejewicz. Post-mortem iris recognition with deep-learning-based image segmentation. *Image and Vision Computing*, 94:103866, 2020.
- [36] A. Czajka, D. J. Chute, A. Ross, P. J. Flynn, and K. W. Bowyer. Software tool and methodology for enhancement of unidentified decedent systems with post-mortem automatic iris recognition. *New York, 2019-2021. Inter-university Consortium for Political and Social Research [distributor]*, 2023.
- [37] K. Simonyan and A. Zisserman. Very deep convolutional networks for large-scale image recognition. *arXiv preprint arXiv:1409.1556*, 2014.
- [38] G. Huang, Z. Liu, L. Van Der Maaten, and K. Q. Weinberger. Densely connected convolutional networks. In *Proceedings of the IEEE Conference on Computer Vision and Pattern Recognition*, pages 4700–4708, 2017.
- [39] K. He, X. Zhang, S. Ren, and J. Sun. Deep residual learning for image recognition. In *Proceedings of the IEEE Conference on Computer Vision and Pattern Recognition*, pages 770–778, 2016.
- [40] C. Szegedy, V. Vanhoucke, S. Ioffe, J. Shlens, and Z. Wojna. Rethinking the inception architecture for computer vision. In *Proceedings of the IEEE Conference on Computer Vision and Pattern Recognition*, pages 2818–2826, 2016.

- [41] M. Trokielewicz, A. Czajka, and P. Maciejewicz. Post-mortem iris recognition with deep-learning-based image segmentation. *Image and Vision Computing*, 94:103866, 2020.
- [42] M. Trokielewicz, A. Czajka, and P. Maciejewicz. Post-mortem iris recognition resistant to biological eye decay processes. In *2020 IEEE Winter Conference on Applications of Computer Vision (WACV)*, pages 2296–2304, 2020.
- [43] R. A. Bhuiyan and A. Czajka. Forensic iris image synthesis. *Proceedings of the IEEE/CVF Winter Conference on Applications of Computer Vision*, pages 1015–1023, 2024.

## Forensic Iris Image-Based Post-Mortem Interval Estimation Supplementary Materials

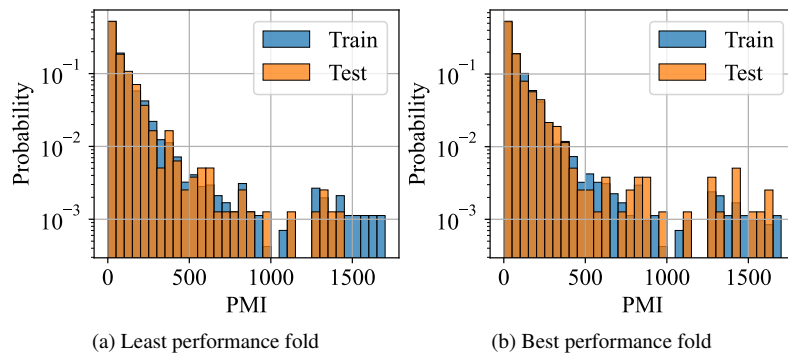


Figure A1. Comparison of the PMI distributions between training and test datasets for the least (a) and best (b) performing folds observed in the **sample-disjoint** 10-fold cross-validation for the **NIR data**.

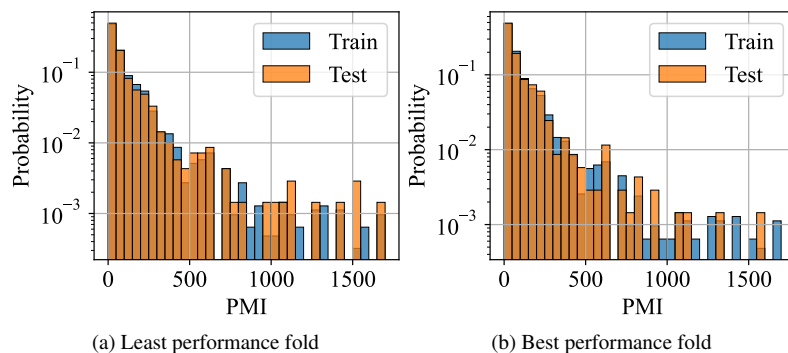
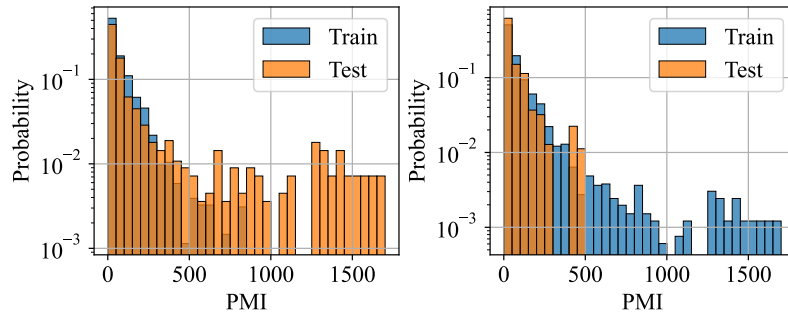


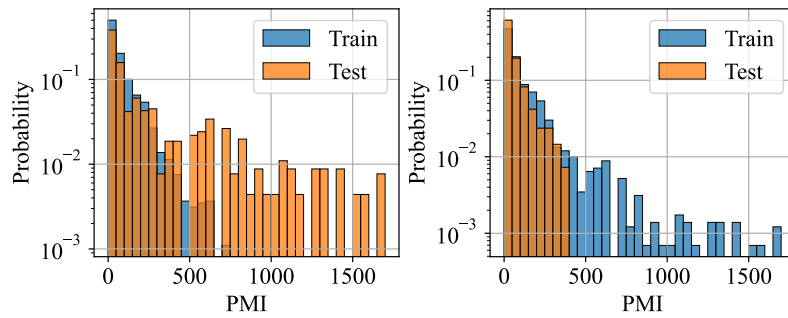
Figure A2. Same as in Fig. A1 but for **RGB data**.



(a) Least performance fold

(b) Best performance fold

Figure A3. Comparison of the PMI distributions between training and test datasets for the least (a) and best (b) performing folds observed in the **subject-disjoint** 10-fold cross-validation for the **NIR data**.



(a) Least performance fold

(b) Best performance fold

Figure A4. Same as in Fig. A3 but for **RGB data**.

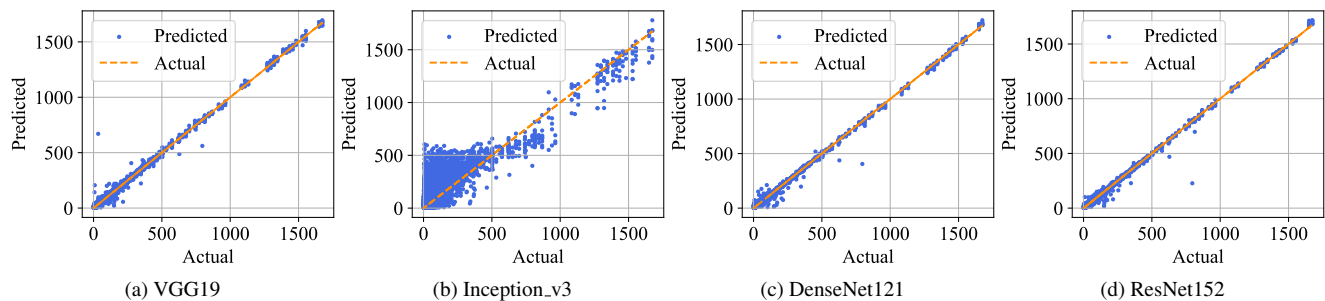


Figure A5. Scatter plots visualizing the predicted PMI values against the actual PMI values for **NIR data** combined for all **sample-disjoint** 10-fold cross-validations.

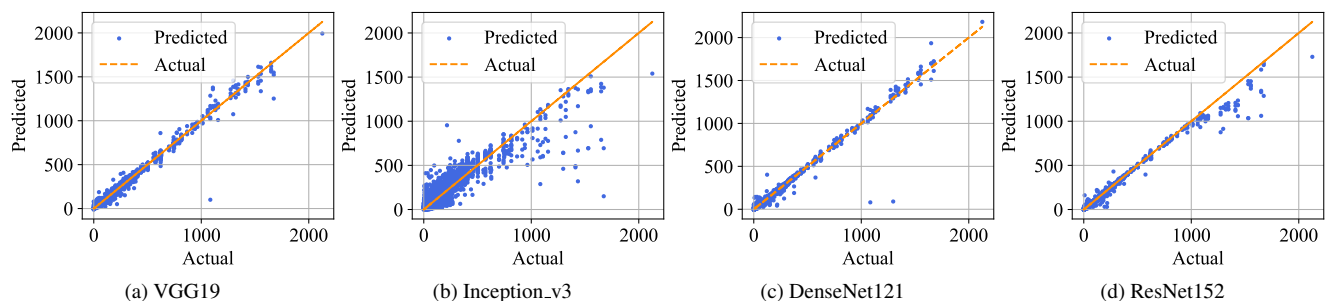


Figure A6. Scatter plots visualizing the predicted PMI values against the actual PMI values for **RGB data** combined for all **sample-disjoint** 10-fold cross-validations.

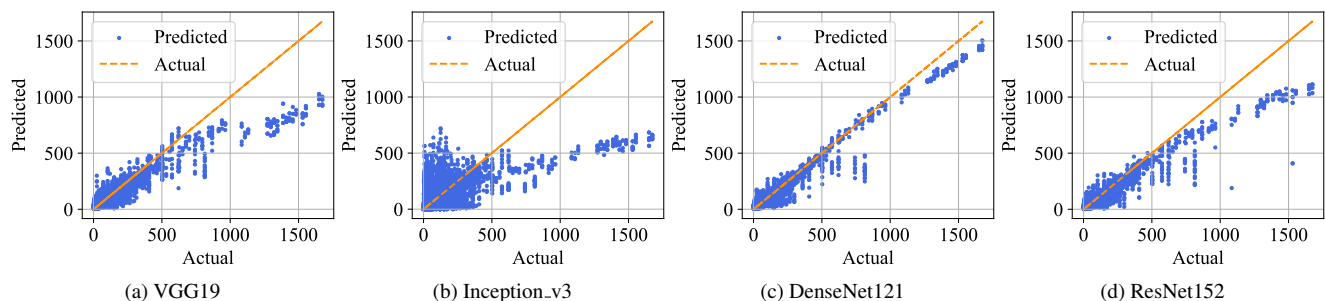


Figure A7. Scatter plots visualizing the predicted PMI values against the actual PMI values for **NIR data** combined for all **subject-disjoint** 10-fold cross-validations.

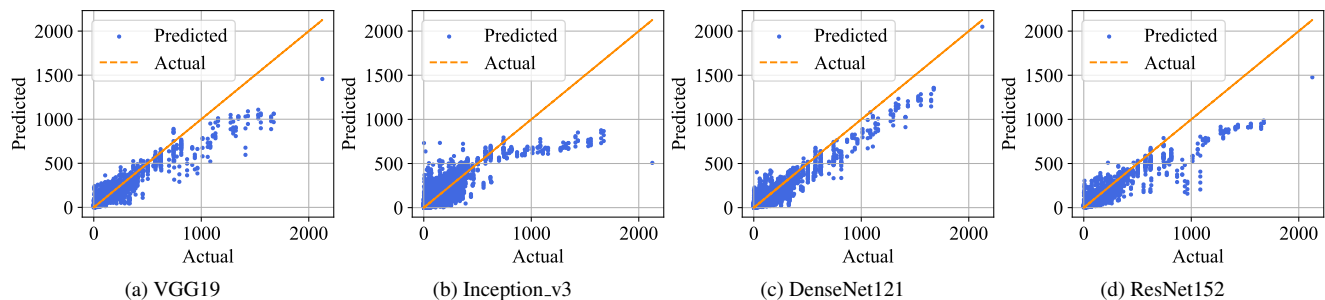


Figure A8. Scatter plots visualizing the predicted PMI values against the actual PMI values for **RGB data** combined for all **subject-disjoint** 10-fold cross-validations.

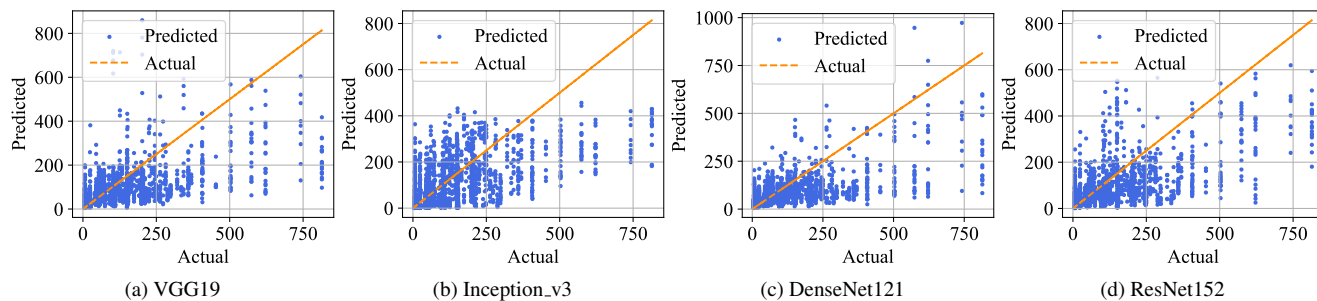


Figure A9. Scatter plots visualizing the predicted PMI values against the actual PMI values for **NIR data** by models trained on the NIJ dataset and **tested on the Warsaw dataset**.

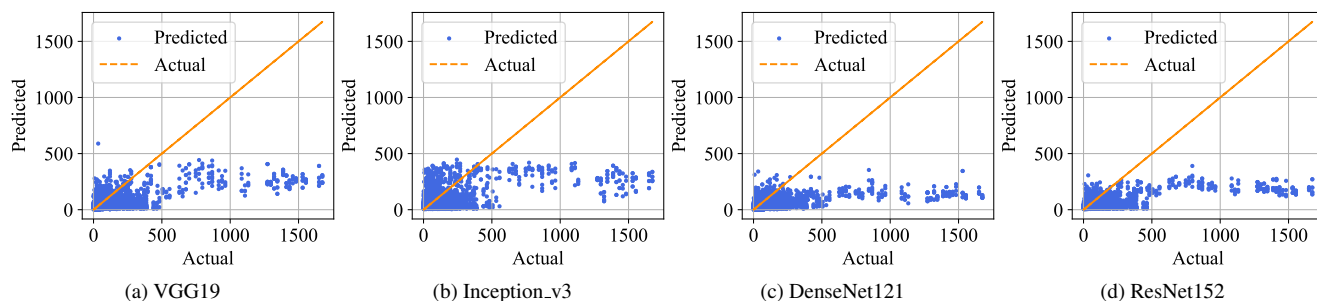


Figure A10. Scatter plots visualizing the predicted PMI values against the actual PMI values for **NIR data** by models trained on the Warsaw dataset and **tested on the NIJ dataset**.

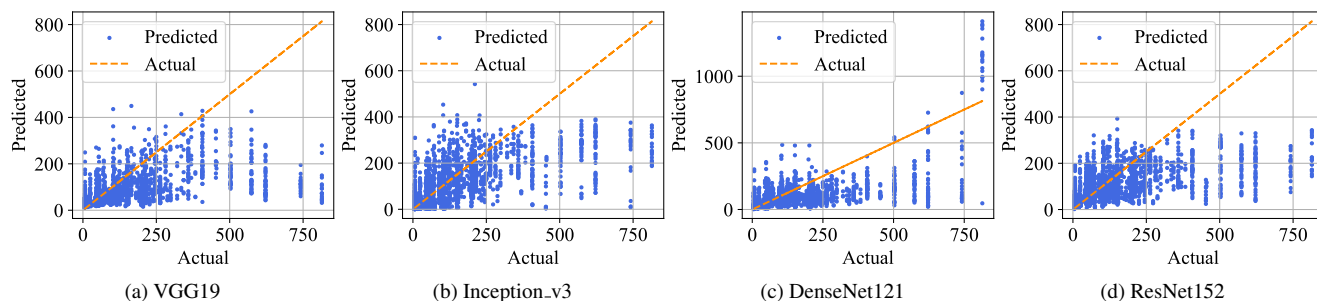


Figure A11. Scatter plots visualizing the predicted PMI values against the actual PMI values for **RGB data** by models trained on the NIJ dataset and **tested on the Warsaw dataset**.

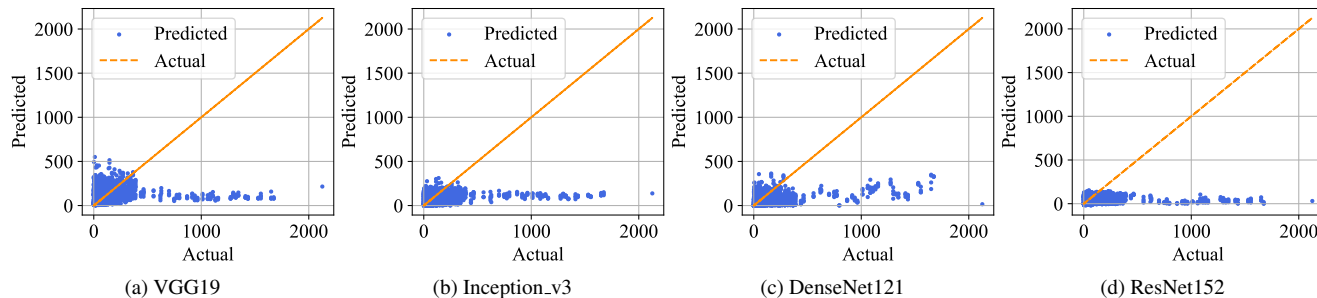


Figure A12. Scatter plots visualizing the predicted PMI values against the actual PMI values for **RGB data** by models trained on the Warsaw dataset and **tested on the NIJ dataset**.